


 Cite this: *RSC Adv.*, 2023, **13**, 2795

# Deep learning for automated size and shape analysis of nanoparticles in scanning electron microscopy

 Jonas Bals and Matthias Eppe \*

The automated analysis of nanoparticles, imaged by scanning electron microscopy, was implemented by a deep-learning (artificial intelligence) procedure based on convolutional neural networks (CNNs). It is possible to extract quantitative information on particle size distributions and particle shapes from pseudo-three-dimensional secondary electron micrographs (SE) as well as from two-dimensional scanning transmission electron micrographs (STEM). After separation of particles from the background (segmentation), the particles were cut out from the image to be classified by their shape (e.g. sphere or cube). The segmentation ability of STEM images was considerably enhanced by introducing distance- and intensity-based pixel weight loss maps. This forced the neural network to put emphasis on areas which separate adjacent particles. Partially covered particles were recognized by training and excluded from the analysis. The separation of overlapping particles, quality control procedures to exclude agglomerates, and the computation of quantitative particle size distribution data (equivalent particle diameter, Feret diameter, circularity) were included into the routine.

Received 7th December 2022

Accepted 10th January 2023

DOI: 10.1039/d2ra07812k

[rsc.li/rsc-advances](http://rsc.li/rsc-advances)

## Introduction

Many products contain micro- or nanoscale powder materials. Such materials must be analysed with high precision for any application with respect to particle size and particle shape distribution. A common method for the analysis of particles is scanning electron microscopy (SEM).<sup>1</sup> SEM can be operated in different modes, *i.e.* secondary electron detection mode (SE) and scanning transmission electron mode (STEM). SE images have a high field of depth and are especially well suited to show surface details, including the surface topography in a pseudo-three-dimensional representation. STEM images have a higher spatial resolution and give a two-dimensional representation of particles. The images generated by these two modes are fundamentally different in terms of their pixel intensity distribution and overall appearance. Therefore, an automated image analysis needs different approaches to deal with SE and STEM images, respectively.

Usually, SEM images are analysed by experienced human reviewers to count and measure the depicted particles, *e.g.* to determine the particle size distribution of a given sample.<sup>2</sup> Another particle property which is generally of interest is the particle shape. If images show an assembly of particles with different shapes, their classification into different categories (*e.g.* sphere, cube, rod, or triangle) is usually done manually. This is a time-consuming process which may be biased by a human reviewer.<sup>3</sup> To accomplish a fast and objective analysis,

there is a strong need for non-biased, rapid methods to analyse SEM images.<sup>4</sup>

Machine learning has been applied to detect and identify objects of high variability in SEM images.<sup>5,6</sup> In principle, this permits a more objective and usually much faster analysis than a human assessment.<sup>7-12</sup> Semantic segmentation of images into coherent areas of the same class (*e.g.* foreground and background) is possible by convolutional autoencoders (CNNs) like the UNet architecture.<sup>13</sup> UNet and its various developments were highly successful in biomedical image processing, and several attempts were made to apply it to nanoparticle analysis as well.<sup>14</sup> Further efforts to classify particles according to their shape were carried out by dedicated classification networks.<sup>15,16</sup>

The workflow presented here includes two steps performed by convolutional neural networks (CNN) to accomplish a full analysis of SEM images of nanoparticles. The first step is to label each pixel as either foreground or background (segmentation). Coherent areas of foreground pixels (“particles”) are then cut out and processed by a second neural network to determine the shape of the individual particle (classification). In this step, partially covered particles are identified and removed from the classification. A subsequent analysis of particle size, diameter, and circularity of all particles shown in an image is finally performed.

## Results and discussion

Training a neural network leads to a model which is adapted to a given dataset after training on a representative set of features

*Inorganic Chemistry, Centre for Nanointegration Duisburg-Essen (CENIDE), University of Duisburg-Essen, 45117 Essen, Germany. E-mail: matthias.eppe@uni-due.de*



from this dataset. This model, in our case a convolutional neural network, recognizes features within the dataset and learns to correlate these features with an associated class. The associated class is denoted as label. In the segmentation, these labels are given for each pixel and can be either foreground or background. In the shape classification, a case label describes the shape of a given particle (e.g. cube or sphere). In each training step an image shown to the network generates an output which is a probability distribution over all possible cases. A segmentation network will calculate the probability for each pixel to be either foreground or background. A classification network will calculate a probability for each particle to belong to a shape class of the training dataset. This probability distribution is then compared with the true output, *i.e.* the ground truth.<sup>5,14,17,18</sup>

The loss function measures the difference between prediction and true label. A small difference between prediction and true label leads to a small loss and a better performance of the network. Each presentation of all images of a given training dataset to the network is called an epoch. The network parameters are changed several times during one epoch. The adaptation is performed after a mini-batch (a part) of images has been shown to the network. An optimizer algorithm uses the loss function to gradually adjust the parameters of the network. A high loss results in a strong adaptation of the network parameters. Training ends when the network is no longer improving its adaption to the training data, *i.e.* the loss function does not further decrease. This can require several hundred training epochs.<sup>19</sup>

Two different workflows were generated here, one for SE images and one for STEM images. This was necessary because the image types represented by SE and STEM images are strongly different. Both workflows shared the UNET++ architecture for segmentation.<sup>20</sup>

### Training procedure for segmentation

SEM images usually show two-dimensional representations of particles having a three-dimensional shape. Of course, geometric information is lost by such a projection. This is often tacitly ignored, *e.g.* circular particles are assumed to be spherical, quadratic particles are assumed to be cubic, *etc.* In fact, a circular particle may also be disc-like because particles are usually settling on their largest face during sample preparation for SEM. This will lead to images where most discs are sitting on their circular face instead of their edge. This is a fundamental problem which can only be addressed by recording SEM data taken from different angles.

The segmentation training dataset consisted of 30 SE and 12 STEM images, respectively. We also used 32 SE images published by Ruehle *et al.*<sup>21</sup> Validation datasets contained 16 SE images and 3 STEM images, respectively. These images had typical sizes of 2000 × 1600 pixels. The particles in both image types were typically separated by 1 to 3 pixels, *i.e.* the particle density was high (as common in scanning electron microscopy).

Because the input of UNet++ was fixed to 512 × 512 pixels, we randomly cut out patches of the training images. For data

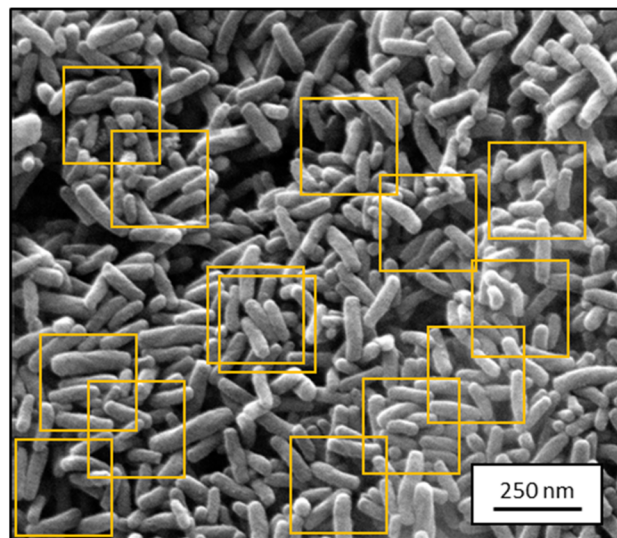


Fig. 1 Representative SEM image from the training dataset for segmentation containing ZnO nanorods (2048 × 1886 pixels; SE mode). Orange boxes show typical cut-out patches used for training.

augmentation, we artificially altered each image by random rotation, flipping, intensity variation, shearing, and zooming (up to 15% each) before cutting out image patches. The number of patches per image depended on the image size. Bigger images resulted in more patches. Approximately 450 patches were cut out of the 30 SE images. Approximately 180 patches were cut out of the 12 STEM images. The random extraction of patches from each image was performed in each epoch. An epoch was finished after each patch of each image was processed once by the CNN. Fig. 1 illustrates this step.

### Segmentation of SEM images by UNet++

Since its introduction by Ronneberger *et al.* in 2015, UNET has demonstrated its usefulness for the segmentation of medical images.<sup>13</sup> We applied the improvement of UNet, *i.e.* UNet++,<sup>20,22</sup> to a wide range of different SEM images. The major difference between UNET and UNet++ is the link between encoder and decoder *via* nested dense convolutional layers which enhances semantic segmentation.<sup>23</sup> The network weights were changed after each patch.

Several problems emerge when training a neural network with SE and STEM images of nanoparticles.

First, in STEM images, the particles can touch or overlap and even form continuous aggregates (agglomerates) with no separating background between them. These aggregates cannot be separated into individual particles. For a precise size analysis, agglomerates must therefore be excluded.<sup>3</sup> We achieved this by explicitly training the classification network to identify agglomerates.

Second, in SE images, the particles can also overlap but borders of particles are usually well distinguishable. The particles are separated by a thin line, sometimes as narrow as one pixel.



Third, particles in SE images can be present in different intensities ranging from dark (overshadowed particles) to bright (particles close to the electron detector; see Fig. 1). The neural network must adapt to these differences.

The problem extends to overlapping particles. Humans tend to impose an expected geometry to a partially covered particle, e.g. by assuming that a particle of which 80% are seen as sphere is implicitly considered as a sphere. However, if there is no information on the missing 20%, this assumption is based on subjective expectations and not on experimental data. Of course, no method can supplement pixels which are not visible because they are behind another particle in the front. In that case, the true particle shape (ground truth) is unknown.

The preparation of samples is therefore decisive to obtain good segmentation and classification results. A low particle density on the sample holder usually leads to well separated particles. Nevertheless, the assessment of a large number of particles (>1000) is necessary to ensure a reliable statistical representation of a given sample. Unfortunately, images showing many overlapping particles (often by solvent evaporation during sample preparation) are most common when particles are depicted by SEM (see Fig. 1).

Ronneberger *et al.* introduced weight loss maps to overcome the problem of a narrow separation of objects.<sup>13</sup> Weight loss maps are matrices of the same size as the image that give each pixel an individual weight. In our case, the weight of each background pixel is given by its distance to the next particle edge (distance-based weight loss maps). These pixels are particularly important to separate adjacent particles. By giving these separating background pixels a higher weight, we forced the neural network to focus on the immediate background around each particle (Fig. 2). Weight loss maps were computed for ground truth annotation masks which were manually prepared before the network was trained. Due to the higher weights for separating background pixels between particles, the network predominantly learned to segment those areas. Thus, in the application of networks to any new image, no weights

were needed because the network was already sensibilized (*i.e.* trained) to those areas. Notably, calculating weight maps requires considerable computing time.

In STEM images, background pixels between two touching particles can be very bright (see Fig. 2-A2). The model erroneously merges such particles because it cannot identify a separating border between them. To train the model to distinguish between bright background and particles we included the image intensity into the training process. The combination of distance-based weight loss maps and the pixel brightness led to a model which successfully separated touching particles. We denote this approach intensity-based weight loss maps in the following. Eqn (1) shows the modified version of Ronneberger *et al.*<sup>13</sup> for the weight of each pixel  $w(x)$

$$w(x) = w_0 \times \exp\left(-\frac{(d_1(x) + d_2(x))^2}{2\sigma^2}\right) + \gamma \times I_c(x) + 1 \quad (1)$$

with  $d_1(x)$  and  $d_2(x)$  the distance of background pixel  $x$  to the edge of the nearest two particles.  $w_0$  and  $\sigma$  are adjustable parameters, and  $\gamma \times I_c(x)$  is the normalised intensity of pixel  $x$  multiplied by a factor gamma. The first term in the equation results in a distance-based weight loss map which was used for SE images. The addition of the second part leads to intensity-based weight loss maps which were used for STEM images. We set the parameters to  $w_0 = 10$ ,  $\sigma = 7$  and  $\gamma = 2$  where the best results were obtained. In the case of SE images, the term  $\gamma \times I_c(x)$  was not used ( $\gamma = 0$ ) because the intensity variations did not have the same strong effect on the segmentation as in the STEM images.

### Segmentation results

Segmentation results of the validation dataset are shown in Table 1. As reference we used the default UNet architecture trained on the same data. Experiments for both types of weight loss maps were carried out for SE and STEM images. We used intensity-based weight loss maps for STEM images and distance-based weight loss maps for SE images, respectively. We validated each model with different metrics. Abbreviations used in eqn (2)–(7) refer to the following: TP – True Positive, FP – False Positive, TN – True Negative, FN – False Negative. These metrics can be used in segmentation and classification. In terms of segmentation each pixel is counted, while in terms of classification each image of a particle is counted.

$$\text{Precision} = \frac{\text{TP}}{\text{TP} + \text{FP}} \quad (2)$$

$$\text{Recall} = \frac{\text{TP}}{\text{TP} + \text{FN}} \quad (3)$$

$$\text{Accuracy} = \frac{\text{TP} + \text{TN}}{\text{TP} + \text{FP} + \text{TN} + \text{FN}} \quad (4)$$

$$\text{Intersection over Union (IoU)} = \frac{\text{TP}}{\text{TP} + \text{FP} + \text{FN}} \quad (5)$$

$$F1 = \frac{2 \times \text{TP}}{2 \times \text{TP} + \text{FP} + \text{FN}} \quad (6)$$

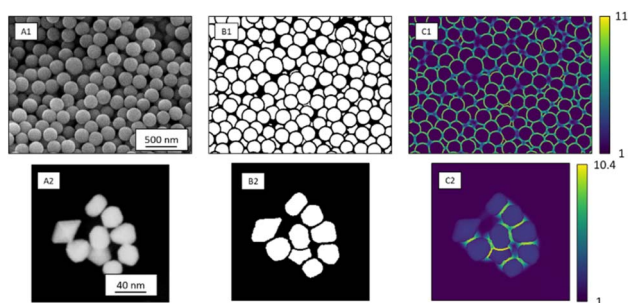


Fig. 2 SE image depicting SiO<sub>2</sub> microspheres (A1) with corresponding segmentation map (B1), and distance-based weight loss map calculated by eqn (1) (C1). STEM image of Au nanoparticles (A2) with segmentation map (B2) and intensity-based weight loss map (C2). Each background pixel (black) of the segmentation map was assigned with an individual weight loss depending on the distance to the edges of the two nearest particles. These weights varied between 1 and 11 for SE images and 1 and 13 for STEM images. The general weight of foreground pixels (white) was 1.





**Table 1** Segmentation results for SE and STEM images, respectively. The table includes two kinds of metrics. The regular segmentation metrics uses the whole ground truth segmentation map and the model prediction, *i.e.* the full image. The “particles only” metrics ignores most of the background. It compares only areas of the image which are part of the particle bounding boxes. Therefore, it compares how well the individual particles and the directly enclosing background of particles are segmented.<sup>21</sup> The given errors represent confidence intervals

CNN	Type	Precision	Recall	Accuracy	IoU	F1	Pixel error	Rand error
Unet	SE (distance-based weight loss maps)	97 ± 1%	97 ± 2%	97 ± 2%	94 ± 2%	97 ± 1%	3 ± 2%	2 ± 1%
	STEM (intensity-based weight loss maps)	96 ± 4%	93 ± 5%	99.5 ± 0.5%	90 ± 6%	94 ± 3%	0.5 ± 0.5%	1.0 ± 0.9%
Unet++	SE (distance-based weight loss maps)	97 ± 1%	96 ± 5%	97 ± 7%	93 ± 2%	96 ± 5%	3 ± 3%	2 ± 2%
	SE (intensity-based weight loss maps)	98 ± 2%	93 ± 3%	96 ± 2%	91 ± 3%	95 ± 1%	4 ± 12%	3 ± 16%
	SE (particles only)	98 ± 2%	95 ± 3%	94 ± 2%	93 ± 3%	96 ± 1%	13 ± 12%	18 ± 16%
	STEM (distance-based weight loss maps)	96 ± 4%	91 ± 7%	99 ± 1%	88 ± 1%	93 ± 7%	1 ± 4%	1.1 ± 0.6%
	STEM (intensity-based weight loss maps)	96 ± 6%	96 ± 4%	99.7 ± 0.4%	92 ± 7%	96 ± 4%	0.3 ± 0.4%	1 ± 1%
	STEM (particles only)	99 ± 1%	96 ± 4%	96 ± 3%	94 ± 4%	97 ± 2%	13 ± 28%	8 ± 12%

$$\text{Pixel error} = 100 - \text{accuracy} \quad (7)$$

In addition, we calculated the Rand error.<sup>24</sup> The Rand error measures the degree in which two segmentations (the true label and the model prediction) disagree whether a given pixel belongs to the same object in both segmentations. Therefore, the Rand error measures how well particles are separated, with 0% indicating a good separation and 100% an unsuccessful separation.

The introduction of intensity-based weight loss maps significantly improved the segmentation performance of UNet++ for STEM images. However, SE images did not benefit from the application of intensity-based weight loss maps. SE images usually have a wide distribution of grayscales. In SE images, background and particles share the same range of pixel intensity, whereas in STEM images background and particles are strongly different (two distinct peaks of pixel intensities). The background between touching particles in STEM can reach the same intensity as the particles. This is not the case for SE images where particles often surrounded by a darker rim due to lower electron excitation. The models UNet and UNet++ performed almost equally on both types of images. UNet++ uses only 7.7 million parameters compared to 31 million parameters of UNet.<sup>25</sup> Thus, it is much faster than UNet without compromising the segmentation ability. Overall, the segmentation procedure was very efficient. The introduction of intensity-based weight maps led to a significant improvement in the IoU by 4% for STEM images. This is due to the better separation of touching particles by segmentation of background pixels.

### Shape classification

Segmentation of images is only the first step of analysis. Next, parameters that describe particle size and shape are of interest.

The classification of single particles was performed by two different CNNs: Alexnet for STEM images and ResNet34 for SE images. We initialized both networks according to He *et al.*<sup>26</sup> As optimizing algorithm, we used ADAM<sup>27</sup> with the default settings of Tensorflow.<sup>28</sup> As loss function, we used the cross-entropy loss function introduced by Fisher.<sup>29</sup> Both networks were tested against their validation dataset.

After segmentation of raw particles from the background, the particle bounding boxes were slightly enlarged and cut out from the SEM image. For each particle, the cut-out area was larger than the close-fitting bounding box to provide surrounding information for the following classification network (Fig. 3). As classification networks, we used AlexNet for STEM images because of the limited data (<1000 images per class).<sup>19</sup> Larger networks require a more variable dataset which was not available for STEM images. A variation in terms of particle orientation and colour distribution is not given in STEM images which are just 2D representations with a very limited distribution of either very dark (background) or very bright (particle) grayscales. For SE images, the larger ResNet34 was the preferred option due to its performance in the ILSVRC 2015.<sup>30</sup> For the even deeper variants like ResNet50, we observed

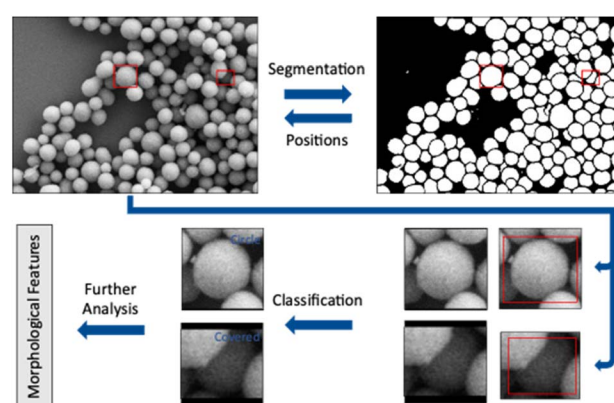


**Fig. 3** The input SEM image (SE mode) is segmented by a UNet++ model. The dimensions of all foreground objects (white coherent areas) were defined by their enclosing bounding box (red boxes) in the segmentation map. The cut-out areas in the SEM image were slightly larger than the bounding boxes to provide additional background information around each object. The image patches were resized until each side of the patch was 224 pixels long because the classification network used only square images. The additional pixels were filled with zero-pixel values (zero-padding; black). The classification model took these square images and assigned each particle to a class (upper row: a circle). If the image contained a particle which was partially covered, this particle was assigned to the class “covered” and excluded from further shape classification (bottom row).



a lack of data variation. We were not able to train ResNet50 to the same extent as it was possible with ResNet34.

### Shape classification of particles from STEM images by AlexNet

For the shape classification of single particles from STEM images, a modified AlexNet architecture was used. This network was developed by Zeiler and Fergus<sup>31</sup> and modified by us by reducing the number of channels in the fully connected layers by a factor of two. In total, 3000 manually classified single images of gold and silver nanoparticles in the classes circle, rod, triangle, square, pentagon, hexagon, agglomerate, and covered were used for training (ground truth). The class “covered” consisted of manually identified particles that were partially covered by other particles in the foreground. The network was specifically trained to recognize these by suitable training images of partially covered particles. Similarly, the class “agglomerate” created and trained with suitable images. Images of single particles were resized to  $224 \times 224$  pixels, while preserving the aspect ratio as depicted in Fig. 3. Data augmentation similar to the segmentation training was applied by random cropping, rotation, and flipping to increase the training dataset. Gaussian noise was also applied for data augmentation by adding a matrix of random values to the image. Class weighing was applied to take different numbers of images in the individual classes into account, using standard procedures.

### Shape classification of particles from SE images by ResNet34

The analysis of single particles from SE images was performed by ResNet34.<sup>16</sup> Altogether, 17 000 images of manually classified  $\text{SiO}_2$ , ZnO, Ag, Au, and  $\text{TiO}_2$  nanoparticles in the classes sphere, sphere-like, cube, rod, and covered particles were used (80% for training, 20% for validation; ground truth). Two different classes for spherical objects were introduced. The class “sphere” comprised round, ball-shaped objects, whereas the class “sphere-like” comprised a range of deformed, elongated, and indented particles. Data augmentation and class weighing was performed as with AlexNet (see above).

### Results of shape classification

The shape classification results are shown in Table 2 and Fig. 4. We have labelled the categories corresponding to 3D shapes (SE) or their corresponding 2D projections (STEM) according to Munoz-Marmol *et al.*<sup>32</sup> The mean accuracy (eqn (4)) of the validation dataset for particles imaged by SE and classified by ResNet34 was 93%, and for particles imaged by STEM and classified by AlexNet 95%.

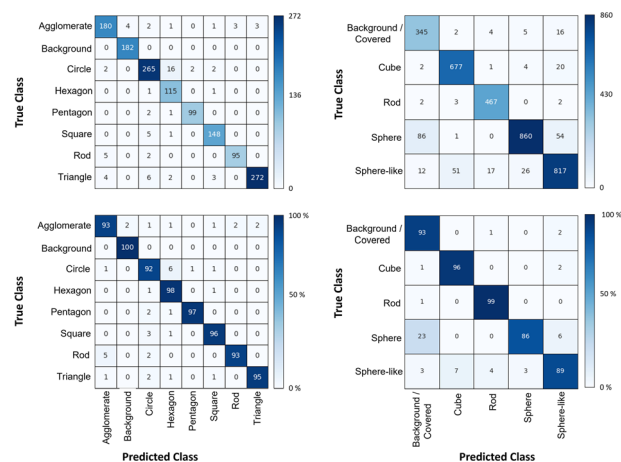


Fig. 4 Confusion matrix for the shape classification of nanoparticles. Left: results for STEM images; right: results for SE images.

The classification networks were then applied to images which were neither used in training nor in validation. Fig. 5 shows representative results. Because both training datasets contained partially covered particles, both networks were trained to identify and exclude partially covered particles. This

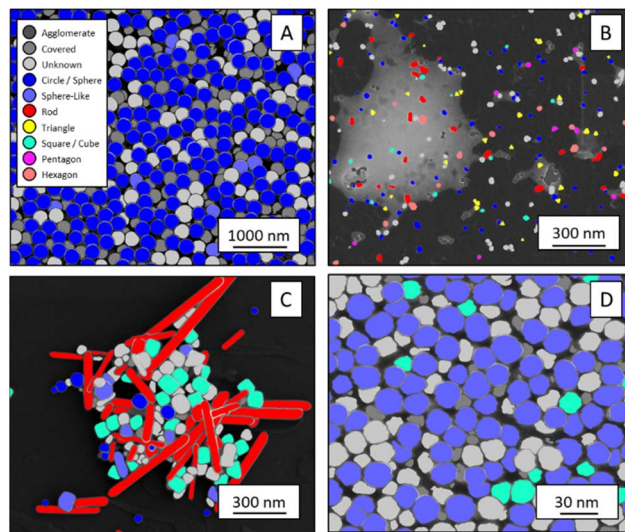


Fig. 5 Representative classification of particles of different materials recorded in SE and STEM modes. The images are illustrative cut-outs from larger images subjected to segmentation and classification. They show nanoparticles of (A):  $\text{SiO}_2$  (SE), (B): Au (STEM), (C): Ag (SE), and (D): ZnO (SE). The full analysis involved the segmentation, followed by classification. The coloured areas are foreground areas (*i.e.* particles) identified by the segmentation and then assigned to a shape class.

Table 2 Accuracy of the classification networks on their validation datasets. Both networks showed an accuracy near or above 90%

Accuracy per class	Covered	Circle/sphere	Sphere-like	Rod	Triangle	Square/cube	Pentagon	Hexagon	Agglomerate	Average
STEM (2D)	97%	96%	—	95%	97%	94%	91%	95%	91%	95%
SE (3D)	93%	86%	89%	99%	—	96%	—	—	—	93%



procedure assured that particles within one class were similar. The shape classification by CNNs gave an overall high accuracy. The application of the validated networks led to an unexpected behaviour when classifying particles whose appearance differed from the trained morphologies. Images of particles with shapes unknown from the training like stars or octahedra showed similar probabilities for many classes, *i.e.* the probability distribution was almost evenly spread among a number of classes. In that case, the classification would have been made by the network based on small differences between the class probabilities (*e.g.* 34% *vs.* 30% *vs.* 28%), *i.e.* decided by a few percent of probability or less. Therefore, as an additional quality control we introduced a confidence limit of 75%. If the probability was below the confidence limit, the particle would be classified as “unknown”. As confidence limit we used the typical human certainty when classifying a given particle of about 75%.<sup>3</sup> Note that the classes for particles identified as “covered” and “agglomerate” (STEM only) were defined as individual classes during training. This assignment was not perfect which is not surprising because there are many different shapes for partially covered or agglomerated particles. The incorporation of partially covered particles into the classification and the subsequent numerical particle analysis would have strongly compromised the resulting data. As typical case, a partially covered circle could appear as sickle-like object, leading to a classification as rod and wrong numerical input data.

In general, SEM images without any covered particles are difficult to acquire as most real images contain covered particles. Thus, some degree of covered particles must be tolerated by any practically applicable classification model. The average false classification rate was 5% for STEM images and 7% for SE images (see Table 2). Thus, covered particles classified by the segmentation model as foreground were classified by a 95% chance for STEM and 93% for SE as background particles/covered particles by the classification model. We consider this as an acceptable error. Furthermore, we did not find deviations in the particle diameter size distributions by including minimally covered particles.

### Numerical data for particle sets

Particle dimensions can be expressed by several methods. Typically, minimum and maximum Feret diameters are used to define particle dimensions. The maximum (or minimum) Feret diameter is the maximum (or minimum) length of a straight line from one end of the particle to another regardless of the orientation. The classification of each particle into a specific

shape class and the exclusion of covered particles made it possible to calculate particle edge lengths/radii directly from their segmented area. We used standard equations to correlate edge length and area for each geometric shape, *e.g.* by using the area of a spherical particle to compute its diameter and its perimeter. Rod lengths can be expressed by the maximum Feret diameter. Together with the area of a rod, the average rod thickness and the aspect ratio can be computed, assuming a rectangular particle shape. Edge lengths for non-spherical objects are useful, *e.g.*, for nanoparticles with distinct aspect ratio. We found a good agreement between human evaluators and the segmentation/classification routine. Table 3 illustrates this for spheres shown in Fig. 5A.

The approach presented here compares well with other methods for image segmentation and classification.<sup>11</sup> We have shown previously that a more classical approach of machine learning using random forest classifier is not capable of nanoparticle segmentation in STEM images.<sup>3</sup> Furthermore, a classification of shapes by principle component analysis of morphological features is not sufficient to distinguish between particles.<sup>33</sup> In general, deep neural networks are superior to shallow classification and regression algorithms like watershed segmentation<sup>34</sup> or custom-made feature detectors<sup>35</sup> for image segmentation or classification as summarized in ref. 36.

## Experimental

### Scanning electron microscopy

SEM micrographs were recorded with two scanning electron microscopes, *i.e.* an Apreo S LoVac (Thermo Fisher Scientific) instrument with a segmented STEM (transmission mode) detector, and a FEI Quanta 400F instrument with a secondary electron (SE) detector. Particle were drop-cast onto carbon-coated copper grids and dried in air. Electrically insulating materials were sputter-coated with AuPd (80 : 20) before SEM analysis.

### Computational hardware and software

Neural network training was performed with an NVIDIA GeForce GTX 1660 on a Lenovo IdeaCentre T540 – 15ICK G Workstation. Images used in final validation were not used in any training. Anaconda 4.10.3 with Python 3.9.7 and Tensorflow/Keras 2.8.0 were used to implement the neural networks. OpenCV Version 4.5.3 was used to calculate particle properties.

**Table 3** Representative analysis of the SE image containing SiO<sub>2</sub> microspheres (cut-out shown in Fig. 5A). After segmentation of the full image, 2425 objects were identified. The particle classification identified 945 objects as partially covered. These covered particles were not considered in the analysis. The remaining 1480 particles were classified. 1360 of them fell into the class “sphere” (equivalent to “circle”)

	Perimeter/nm	Area/nm <sup>2</sup>	Convex hull area/nm <sup>2</sup>	Circularity/—	Minimum Feret diameter/nm	Equivalent circle diameter/nm	Circle diameter by human evaluator/nm
Average	625	35 489	36 625	0.97	204	213	230
Std. dev.	160	4955	4630	0.03	19	14	17
Number of analysed particles	1480	1480	1480	1480	1480	1360	100





## Conclusions

The capability of an automated analysis to classify STEM and SE images of nanoparticles was demonstrated. The workflow used the CNN UNet++ for segmentation and the CNNs AlexNet and ResNet34 for shape classification. The segmentation of SEM images of nanoparticles into coherent foreground areas (particles) and background is possible with high efficiency, and even overlapping or touching particles were often separable. Weight-loss maps based on the distance of background pixels to the particle borders together with the image intensity considerably improved the segmentation of STEM images but did not improve the segmentation of SE images. The intensity variations occurring in an SEM image are usually unavoidable but may be improved by a good sample preparation, *i.e.* a low particle density with few overlapping particles. The performance of UNet++ was comparable to UNet. However, UNet++ was faster due to fewer parameters than in UNet, requiring less computing time. The subsequent classification of individual particles into different shapes gave reliable results. Each coherent foreground area of the segmentation map was assigned to one of the previously defined shape categories. The introduction of a class of partially covered particles into the training procedure considerably improved the classification results. In conclusion, CNNs can be used to obtain statistical information about particles of defined shapes. Tacitly, it is assumed that particles which are excluded from the classification have the same size and shape distribution as those particles included in the analysis. This, however, it is a reasonable assumption.

## Author contributions

Conceptualization: both authors; methodology: both authors; investigation: both authors; programming: J. B.; visualization: J. B.; validation: both authors; writing—original draft preparation: both authors; writing—review: both authors. Both authors have read and agreed to the published version of the manuscript.

## Conflicts of interest

There are no conflicts to declare.

## Acknowledgements

We thank Mrs Qianmin Chen, Mr Rui Guo, Dr Jens Helmlinger, Mrs Aikaterini Karatzia, Dr Mateusz Olejnik, and Dr Kevin Pappert for the synthesis of samples and provision of their images and data. For SEM operation and sample preparation, we are grateful to Tobias Bochmann, Ursula Giebel and Dr Kateryna Loza.

## Notes and references

1 H. Fissan, S. Ristig, H. Kaminski, C. Asbach and M. Epple, *Anal. Methods*, 2014, **6**, 7324–7334.

- 2 M. M. Modena, B. Rühle, T. P. Burg and S. Wuttke, *Adv. Mater.*, 2019, **31**, 1901556.
- 3 J. Bals, K. Loza, P. Epple, T. Kircher and M. Epple, *Materialwiss. Werkstofftech.*, 2022, **53**, 270–283.
- 4 M. H. Modarres, R. Aversa, S. Cozzini, R. Ciancio, A. Leto and G. P. Brandino, *Sci. Rep.*, 2017, **7**, 13282.
- 5 E. A. Holm, R. Cohn, N. Gao, A. R. Kitahara, T. P. Matson, B. Lei and S. R. Yarasi, *Metall. Mater. Trans. A*, 2020, **51**, 5985–5999.
- 6 J. Schmidt, M. R. G. Marques, S. Botti and M. A. L. Marques, *npj Comput. Mater.*, 2019, **5**, 83.
- 7 J. Timoshenko, C. J. Wrasman, M. Luneau, T. Shirman, M. Cargnello, S. R. Bare, J. Aizenberg, C. M. Friend and A. I. Frenkel, *Nano Lett.*, 2018, **19**, 520–529.
- 8 A. B. Oktay and A. Gurses, *Micron*, 2019, **120**, 113–119.
- 9 J. M. Ede and R. Beanland, *Sci. Rep.*, 2020, **10**, 8332.
- 10 M. Ilett, J. Wills, P. Rees, S. Sharma, S. Micklethwaite, A. Brown, R. Brydson and N. Hondow, *J. Microsc.*, 2020, **279**, 177–184.
- 11 H. Kim, J. Y. Han and T. Y. J. Han, *Nanoscale*, 2020, **12**, 19461–19469.
- 12 B. Lee, S. Yoon, J. W. Lee, Y. Kim, J. Chang, J. Yun, J. C. Ro, J. S. Lee and J. H. Lee, *ACS Nano*, 2020, **14**, 17125–17133.
- 13 O. Ronneberger, P. Fischer and T. Brox, *arXiv*, preprint, arXiv:1505.04597, DOI: [10.1007/978-3-319-24574-4\\_28](https://doi.org/10.1007/978-3-319-24574-4_28).
- 14 K. Choudhary, B. DeCost, C. Chen, A. Jain, F. Tavazza, R. Cohn, C. W. Park, A. Choudhary, A. Agrawal, S. J. L. Billinge, E. Holm, S. P. Ong and C. Wolverton, *npj Comput. Mater.*, 2022, **8**, 59.
- 15 A. Krizhevsky, I. Sutskever and G. E. Hinton, *Presented in part at the Proceedings of the 25th International Conference on Neural Information Processing Systems – Volume 1*, Lake Tahoe, Nevada, 2012.
- 16 K. He, X. Zhang, S. Ren and J. Sun, *Presented in part at the 2016 IEEE Conference on Computer Vision and Pattern Recognition (CVPR), 27–30 June 2016*, 2016.
- 17 R. Jacobs, *Comput. Mater. Sci.*, 2022, **211**, 111527.
- 18 K. P. Treder, C. Huang, J. S. Kim and A. I. Kirkland, *Microscopy*, 2022, **71**, i100–i115.
- 19 I. Goodfellow, Y. Bengio and A. Courville, *Deep Learning*, MIT Press, 2016.
- 20 Z. Zhou, M. M. Rahman Siddiquee, N. Tajbakhsh and J. Liang, in *Deep Learning in Medical Image Analysis and Multimodal Learning for Clinical Decision Support*, Springer, 2018, pp. 3–11, DOI: [10.1007/978-3-030-00889-5\\_1](https://doi.org/10.1007/978-3-030-00889-5_1).
- 21 B. Rühle, J. F. Krumrey and V. D. Hodoroba, *Sci. Rep.*, 2021, **11**, 4942.
- 22 Z. Zhou, M. M. R. Siddiquee, N. Tajbakhsh and J. Liang, *IEEE Trans. Med. Imag.*, 2020, **39**, 1856–1867.
- 23 G. Huang, Z. Liu, L. van der Maaten and K. Q. Weinberger, *Presented in part at the 2017 IEEE Conference on Computer Vision and Pattern Recognition (CVPR)*, 2017, pp. 21–26.
- 24 R. Unnikrishnan, C. Pantofaru and M. Hebert, *IEEE Trans. Pattern Anal. Mach. Intell.*, 2007, **29**, 929–944.
- 25 K. M. Saaim, S. K. Afridi, M. Nisar and S. Islam, *Ultramicroscopy*, 2022, **233**, 113437.



- 26 K. He, X. Zhang, S. Ren and J. Sun, *arXiv*, 2015, preprint, arXiv:1512.03385, DOI: [10.48550/arXiv.1512.03385](https://doi.org/10.48550/arXiv.1512.03385).
- 27 D. P. Kingma and J. Ba, *arXiv*, 2015, preprint, arXiv:1412.6980, DOI: [10.48550/arXiv.1412.6980](https://doi.org/10.48550/arXiv.1412.6980).
- 28 M. Abadi, P. Barham, J. Chen, Z. Chen, A. Davis, J. Dean, M. Devin, S. Ghemawat, G. Irving, M. Isard, M. Kudlur, J. Levenberg, R. Monga, S. Moore, D. G. Murray, B. Steiner, P. Tucker, V. Vasudevan, P. Warden, M. Wicke, Y. Yu and X. Zheng, *Presented in Part at the 12th USENIX Symposium on Operating Systems Design and Implementation (OSDI 16)*, Savannah, GA, USA, 2016.
- 29 J. Aldrich, *Stat. Sci.*, 1997, **12**, 162–176.
- 30 K. He, X. Zhang, S. Ren and J. Sun, *arXiv*, 2015, preprint, arXiv:1502.01852, DOI: [10.48550/arXiv.1502.01852](https://doi.org/10.48550/arXiv.1502.01852).
- 31 M. D. Zeiler and R. Fergus, *Presented in Part at the Computer Vision – ECCV 2014*, Cham, 2014.
- 32 M. Munoz-Marmol, J. Crespo, M. J. Fritts and V. Maojo, *Nanomedicine*, 2015, **11**, 457–465.
- 33 A. Hughes, Z. Liu, M. Raftari and M. E. Reeves, *PeerJ*, 2015, **2**, e671v671.
- 34 R. Baiyasi, M. J. Gallagher, L. A. McCarthy, E. K. Searles, Q. Zhang, S. Link and C. F. Landes, *J. Phys. Chem. A*, 2020, **124**, 5262–5270.
- 35 A. F. De Siqueira, F. C. Cabrera, A. Pagamisse and A. E. Job, *Microsc. Res. Tech.*, 2014, **77**, 71–78.
- 36 Y. LeCun, Y. Bengio and G. Hinton, *Nature*, 2015, **521**, 436–444.

